Journal of Alloys and Compounds 509 (2011) 724–730

Contents lists available at ScienceDirect

Journal of Alloys and Compounds

journal homepage: www.elsevier.com/locate/jallcom

Bismuth tungstate nano/microstructures: Controllable morphologies, growth mechanism and photocatalytic properties

Yue Tian, Guomin Hua, Wei Xu, Nian Li, Ming Fang, Lide Zhang*

Key Laboratory of Materials Physics, Anhui Key laboratory of Nanomaterials and Nanostructure, Institute of Solid State Physics, Chinese Academy of Sciences, Hefei 230031, PR China

ARTICLE INFO

Article history:
Received 1 July 2010
Received in revised form 30 August 2010
Accepted 1 September 2010
Available online 21 September 2010

Keywords:
Nanostructured materials
Crystal growth
Catalysis
Scanning electron microscopy

ABSTRACT

A facile hydrothermal process was utilized to synthesize bismuth tungstate (Bi_2WO_6) hierarchical nano/microstructures, by which various morphologies could be achieved, including caddice clew-like, nest-like, flower-like and plate-like nanostructures. From the scanning electron microscopy (SEM) and X-ray diffraction (XRD) analysis, the morphologies and phases of the as-synthesized Bi_2WO_6 exhibited a strong dependence on the pH value of the precursor solutions. Moreover, the formation mechanisms of the controllable assembly of these Bi_2WO_6 nano/microstructures under different pH values were investigated. The photocatalytic performances of Bi_2WO_6 with different morphologies were also discussed, and the nest-like Bi_2WO_6 displayed the best photocatalytic activity due to the effective visible absorption and the large surface areas.

1. Introduction

In recent years, the morphology and size controlled synthesis of materials have attracted much attention due to their unique chemical and physical properties that are relevant to the shape and size [1–6]. Considerable efforts have been devoted to synthesize novel nano- and microstructured materials with various morphologies, such as low-dimensional structures (e.g., rods [7], wires [8,9], belts [10], tubes [11]) and hierarchical structures (e.g., branches [12], urchins [13], hollow spheres [14,15]), for their specific properties and corresponding potential applications. If we could understand the growth mechanism and the shape-guiding process, it is possible to program the system to yield the final crystals with desired shape and crystallinity [16].

Bismuth tungstate (Bi_2WO_6) is a typical n-type direct band gap semiconductor with a band gap of 2.75 eV and has potential applications in electrode materials [17], solar energy conversion [18] and catalysis [19–21]. It has also been found that Bi_2WO_6 could act as a stable photocatalyst for the photochemical decomposition of organic contaminants under visible light irradiation [22]. Furthermore, its unique layered structure may enhance the photoactivity of Bi_2WO_6, in which the transfer of electrons to the surface was enhanced along the layered network [23,24]. Recently, various methods have been reported for the fabrication of Bi_2WO_6 with different morphologies: Xu et al. have prepared Bi_2WO_6 nanoparticles by a solvothermal approach using ethylene glycol as synthesis medium [25]. Wang and co-workers have fabricated square-plate-like Bi_2WO_6 nanoplates via an ultrasonic-assisted process [26]. Dai et al. have produced Bi_2WO_6 hierarchical hollow spheres by a facile hydrothermal route [27]. In addition, the hydrothermal methods are commonly used to synthesize Bi_2WO_6 crystals with various morphologies due to its low cost, simple process, and low reaction temperature. However, few investigations are available concerning the controllable synthesis of Bi_2WO_6 nano/microstructures with different morphologies just by adjusting the pH value of precursor solutions in a simple hydrothermal process. Herein, we report a hydrothermal route for morphology-controlled synthesis of the highly crystalline bismuth tungstate nanostructures. The pH effect on the morphology of Bi_2WO_6 was systematically investigated. And the formation mechanism of Bi_2WO_6 particles was discussed from the viewpoint of the crystal growth kinetics.

2. Experimental

2.1. Materials and synthesis

In a typical procedure, $Bi(NO_3)_3{\cdot}5H_2O$ (5 mmol) was added into a nitric acid solution (1.0 mol L^{-1}, 10 mL) to form a clear solution under magnetic stirring for 30 min at room temperature. Then, 20 mL solution of dissolved 2.5 mmol $Na_2WO_4{\cdot}2H_2O$ and 0.4 g of CTAB was slowly dropped into the solution above. Plenty of white precipitation appeared simultaneously. The diluted NaOH solution (4 mol L^{-1}) was then added to adjust the pH value to 0.5, 2.0, 4.0, 7.0, 9.0 and 11.0, respectively. The mixture solution was then sealed in a 60 mL Teflon-lined stainless steel autoclave and maintained at 180 °C for 20 h. Afterwards, the product was filtrated, and washed several times with absolute alcohol and distilled water, and finally dried at 80 °C for 6 h in the air.

* Corresponding author.
E-mail address: ldzhang@issp.ac.cn (L. Zhang).

0925-8388/$ – see front matter © 2010 Elsevier B.V. All rights reserved.
doi:10.1016/j.jallcom.2010.09.010

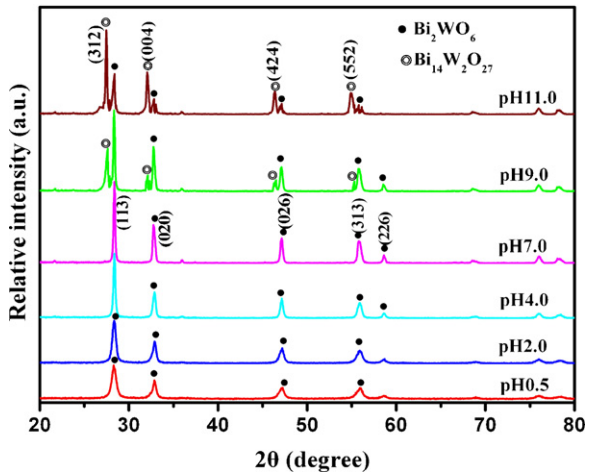

Fig. 1. XRD patterns of Bi_2WO_6 nano/microstructures obtained at different pH values.

2.2. Characterization

X-ray diffraction (XRD) patterns were collected on a Philips X'pert powder X-ray diffractometer with Cu Kα (0.15419 nm) radiation. The morphologies of the products were characterized by field emission scanning electron microscopy (FE-SEM, Sirion 200) operated at an acceleration voltage of 5.0 kV. Transmission electron microscope (TEM) and high-resolution transmission electron microscope (HRTEM) images and selected area electron diffraction (SAED) pattern were obtained on a JEM-2010 microscope using an accelerating voltage of 200 kV.

2.3. Photocatalytic activity test

In order to demonstrate the functionality of the as-prepared Bi_2WO_6 hierarchical nano/microstructures, the photocatalytic activities were evaluated based upon the removal of rhodamine B (RhB) in the aqueous solution. First, same amount (0.2 g) of the as-prepared photocatalyst was respectively immersed into RhB solution (1×10^{-5} M, 100 mL) in darkness for 30 min to establish an adsorption/desorption equilibrium of RhB on the surface of the samples. Subsequently, these solutions were exposed to an optical system composed of a Xe arch lamp (500 W) and a cutoff filter ($\lambda > 400$ nm). At different irradiation time intervals, about 5 mL solutions were collected, and then centrifugalized to remove the photocatalysts. The concentrations of the remnant RhB were monitored by UV–vis spectroscopy at 553 nm.

3. Results and discussion

3.1. XRD phase analysis

Fig. 1 shows the XRD patterns of the products prepared at different pH values. For the samples fabricated at pH 0.5, 2.0, 4.0 and 7.0, the diffraction data obtained match well with the orthorhombic symmetry Bi_2WO_6 crystal phase (JCPDS card no. 73-1126), and

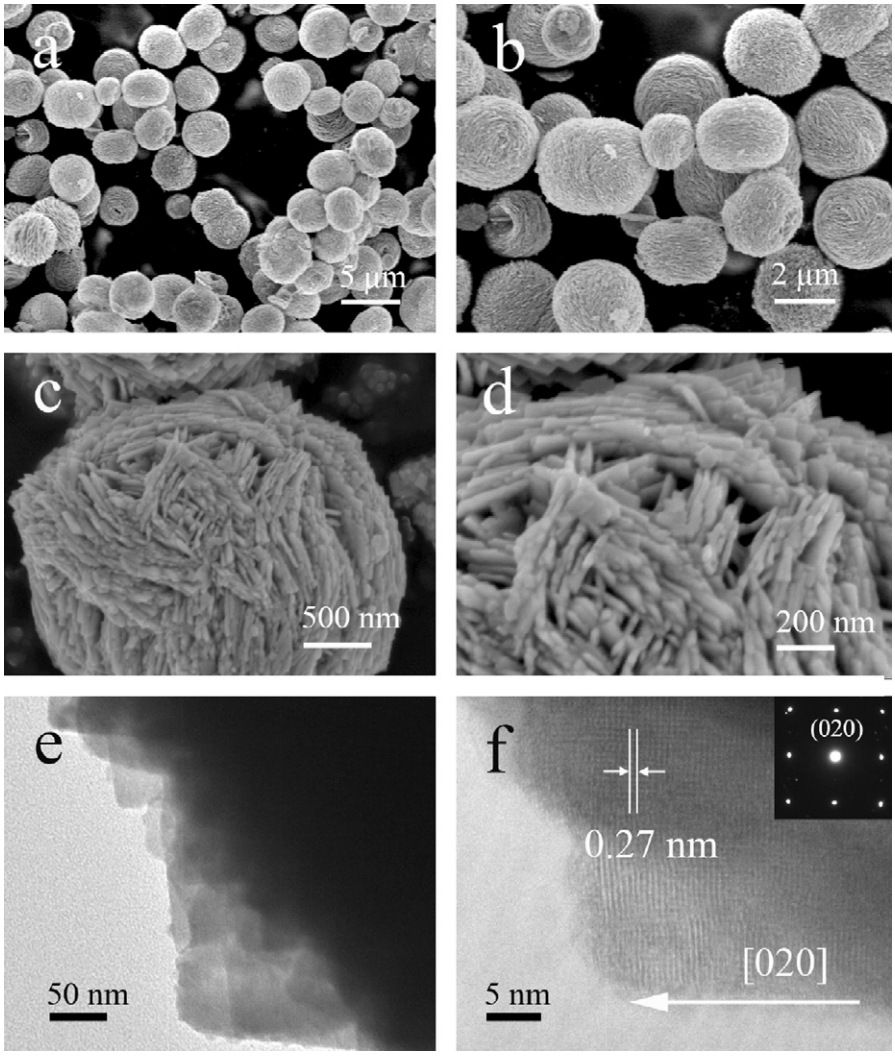

Fig. 2. FE-SEM images (a–d), TEM image (e) and HRTEM image (f) of the caddice clew-like Bi_2WO_6 hierarchical nano/microstructures obtained at pH 0.5. Inset in (f) is a SAED pattern.

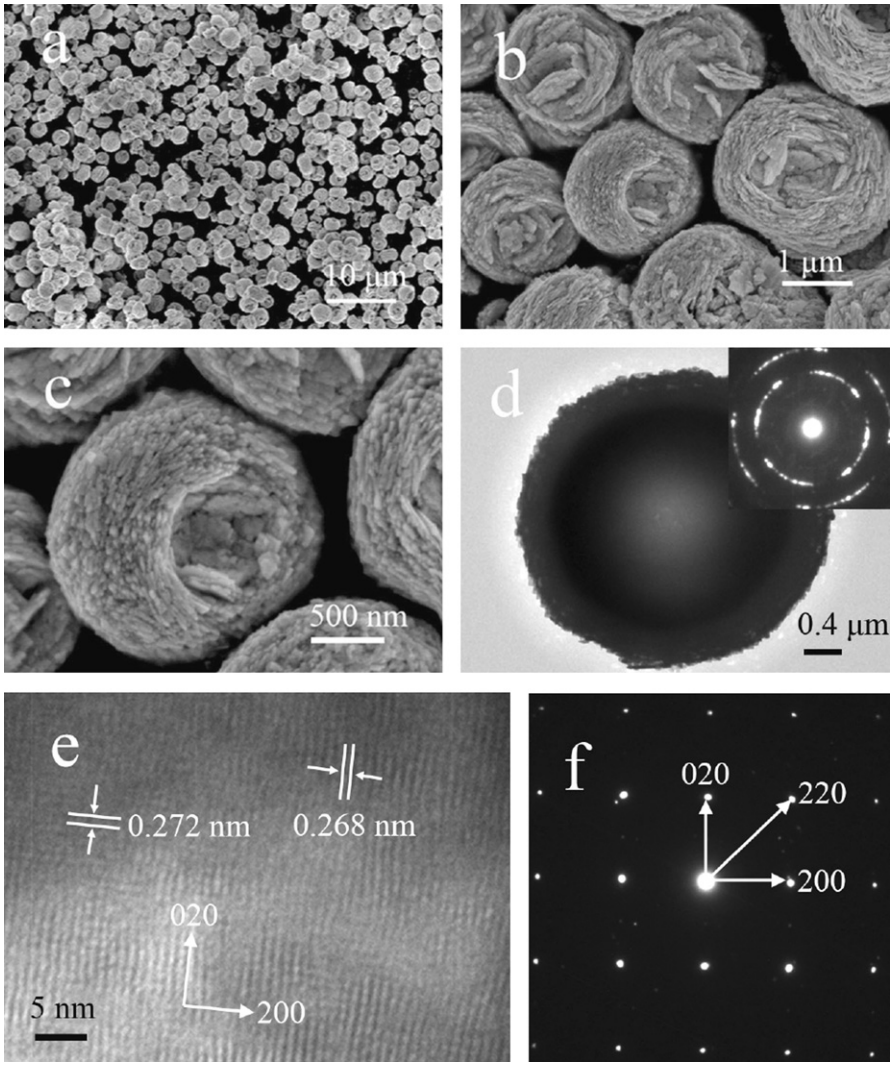

Fig. 3. FE-SEM images (a–c), TEM image (d), HRTEM (e) and (f) SAED pattern of one nanoplate of the nest-like Bi_2WO_6 hierarchical nano/microstructures obtained at pH 2.0.

no peaks of impurities are observed. As the pH value increases to 9.0, the peaks of $Bi_{14}W_2O_{27}$ (JCPDS card no. 39-0061) appear along with those of Bi_2WO_6, which means the sample is a mixture of Bi_2WO_6 and $Bi_{14}W_2O_{27}$. When the pH value increases to 11.0, the peak intensity of $Bi_{14}W_2O_{27}$ increases whereas the peaks intensity of Bi_2WO_6 decreases, which indicates that the $Bi_{14}W_2O_{27}$ crystals become the dominant phase. Based on these evidences, the relevant chemical reactions for Bi_2WO_6 can be formulated as follows:

$$Na_2WO_4 \cdot 2H_2O + 2HNO_3 \rightarrow H_2WO_4 \downarrow + 2NaNO_3 + 2H_2O \quad (1)$$

$$Bi(NO_3)_3 + H_2O \leftrightarrow BiONO_3 + 2HNO_3 \quad (2)$$

$$BiONO_3 + H_2O \leftrightarrow Bi_2O_2(OH)NO_3 + HNO_3 \quad (3)$$

$$Bi_2O_2(OH)NO_3 + H_2WO_4 \rightarrow Bi_2WO_6 + HNO_3 + H_2O \quad (4)$$

However, under the pH values of 9.0 and 11.0, the reaction is illustrated as below:

$$7Bi_2O_2(OH)NO_3 + 2WO_4^{2-} + 3OH^- \rightarrow Bi_{14}W_2O_{27} + 7NO_3^- + 5H_2O \quad (5)$$

Obviously, the pH value of the precursor solution has great influence on the morphology evolution and the purity of the final products, which can be realized through the competition between reactions (4) and (5). It can be clearly seen from these two formulas that low pH value (<7) is favorable for the formation of the Bi_2WO_6 phase in $Bi(NO_3)_3$ and Na_2WO_4. If the pH value is higher than 7, the newly formed $Bi_2O_2(OH)NO_3$ will react with OH^- and WO_4^{2-}, and form the $Bi_{14}W_2O_{27}$ crystals immediately. In addition, the variation in pH values will undoubtedly lead to different amounts of H_2WO_4 precipitation, and finally result in the formation of Bi_2WO_6 with various morphologies. The relevant formation mechanism will be discussed in detail in the following section.

3.2. Morphologies and structures performance

Fig. 2 shows FE-SEM, TEM and HRTEM images of the Bi_2WO_6 nano/microstructures synthesized at pH 0.5. It can be seen obviously that the products have well-defined caddice clew-like structure and uniform size distribution from low-magnification FE-SEM image (Fig. 2a). The average size of the hierarchical Bi_2WO_6 particles is about 3 μm. Through the magnified FE-SEM images (Fig. 2b and c), the hierarchical structure is convoluted by lots of two-dimensional nanoplates. As it can be seen from Fig. 2d, the nanoplates are combined tightly and assembled into caddice clew-like Bi_2WO_6 hierarchical structure. Further investigation is carried out by TEM (Fig. 2e) to reveal the organization of such assembled complex structure. It can be seen that the nanoplates have the length of about 50 nm and the thickness of about 10 nm. A typical HRTEM image of the edge of a Bi_2WO_6 nanoplate (Fig. 2f) shows

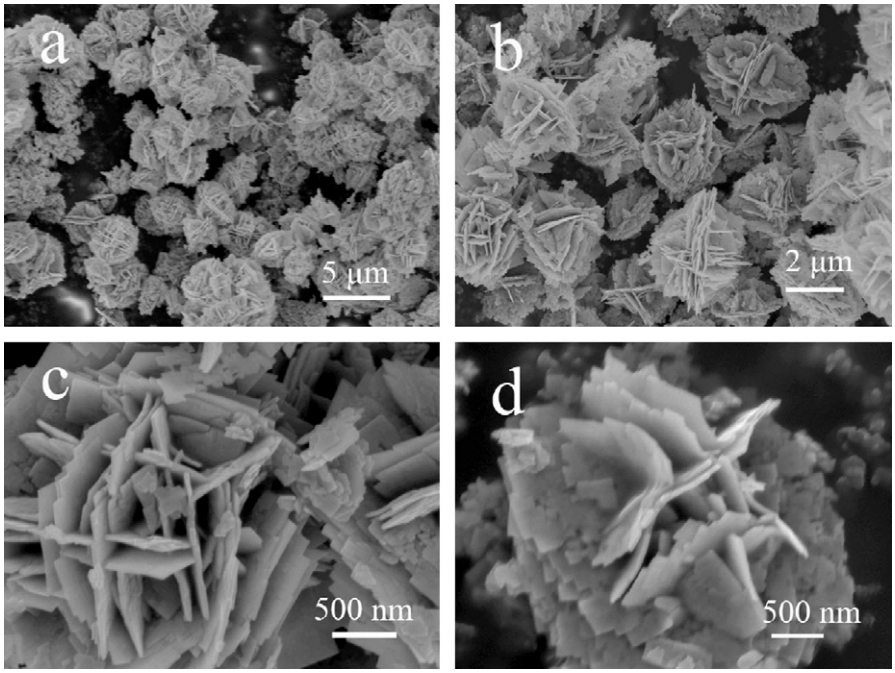

Fig. 4. FE-SEM images of the flower-like Bi_2WO_6 hierarchical nano/microstructures obtained at pH 4.0.

its crystal lattices spacing of 0.27 nm corresponding to the (0 2 0) planes, which indicates that the outer exposed nanoplates of caddice clew-like Bi_2WO_6 grow along the (0 2 0) direction. The bright spots in the SAED pattern (in the inset Fig. 2f) conforms the high crystallinity of the Bi_2WO_6 nanoplate.

When the pH value increases to 2.0 while holding the other conditions constant, the panoramic view of the as-prepared products is shown in Fig. 3a, from which the nest-like hierarchical Bi_2WO_6 particles can be observed. The average size of the particles is measured to be about 3 μm. From the magnified FE-SEM image (Fig. 3b and c), the nanoplates are well-ordered and oriented to form a nest-like hierarchical structure. The morphology of the structure is further investigated by TEM. As shown in Fig. 3d, the observed morphologies are consistent with those from the FE-SEM images, which imply the highly structural uniformity of the as-synthesized product. The light color in the center indicates the hollow structure features of the hierarchical microsphere. The SAED of the whole microsphere (in the inset of Fig. 3d) reveals its weak crystallinity of polycrystalline structure.

Increasing the pH value to 4.0, the morphology of the hydrothermal product is distinctly different. Fig. 4 shows the FE-SEM images of the assembled nano/microstructures. It can be seen that novel uniform flower-like hierarchical Bi_2WO_6 particles with an average size of about 3 μm (Fig. 4a and b) are the main product. Further FE-SEM investigations (Fig. 4c and d) indicate that several plates of about 20 nm in thickness assemble vertically to each other to form a flower-like structure.

As the pH value continues to increase in Fig. 5, nanoplate-like products can be found, and there are fewer connections among the nanoplates. When the pH value reaches 7.0, the three-dimensional structures are fallen apart. The square nanoplates of Bi_2WO_6 are randomly piled up with no typical aggregation observed from the FE-SEM images (Fig. 5a and b). For the sample synthesized at pH 9.0, the crystal phase of $Bi_{14}W_2O_{27}$ appears together with the Bi_2WO_6 phase. The morphology of $Bi_{14}W_2O_{27}$ is irregular crystal-like shape with a smaller size (Fig. 5c and d). When the pH value arrives to 11.0, the crystal $Bi_{14}W_2O_{27}$ becomes the dominant phase and shows irregular morphology with diameter of about 500 nm to 1 μm in Fig. 5e and f.

Besides the pH value, the surfactant CTAB is considered to be another important factor to affect the Bi_2WO_6 morphology. To understand whether the addition of surfactant CTAB is necessary for the formation of Bi_2WO_6 hierarchical structures, the well-designed experiments are carried out, and the experimental results are presented in Fig. 6a–d, which show the morphology evolution of the products with different CTAB amount. When no CTAB was added, loose and underdeveloped nest-like structure is obtained, as seen from Fig. 6a. This means that the hierarchical structure can be assembled in the absence of CTAB even though the morphology seems imperfect. With the CTAB amount increasing to 0.2 g, it can be seen that the hierarchical nest structure is developed and the nanoplates that served as the building blocks of the hierarchical structures are combined more tightly in Fig. 6b. Fig. 6c illustrates a perfect image of the nest-like Bi_2WO_6 with further increase of the amount of CTAB (0.5 g). However, excessive CTAB is not beneficial for the formation of the hierarchical Bi_2WO_6 micro/nanostructures (Fig. 6d, 1.0 g of CTAB). So, the morphology perfection of the obtained products can be promoted by the appropriate amounts of CTAB in the solution. Moreover, the major factor influencing on Bi_2WO_6 morphology is the pH value of precursor solution rather than the surfactant CTAB.

3.3. Formation mechanism

From the above-mentioned evidences, the growth mechanism of the as-synthesized hierarchical assembled structures is easily understandable now. A schematic illustration of the growth mechanism is presented in Fig. 7. Initially, Bi_2WO_6 nanoplates are formed in the mixed solution of $Bi(NO_3)_3$, HNO_3 and Na_2WO_4. After heating the solution at 180 °C for 20 h, the self-assembled hierarchical Bi_2WO_6 morphologies are formed by the building blocks of nanoplates. As indicated by Eq. (1), the pH value of precursor solution has a strong influence on the formation of slightly solu-

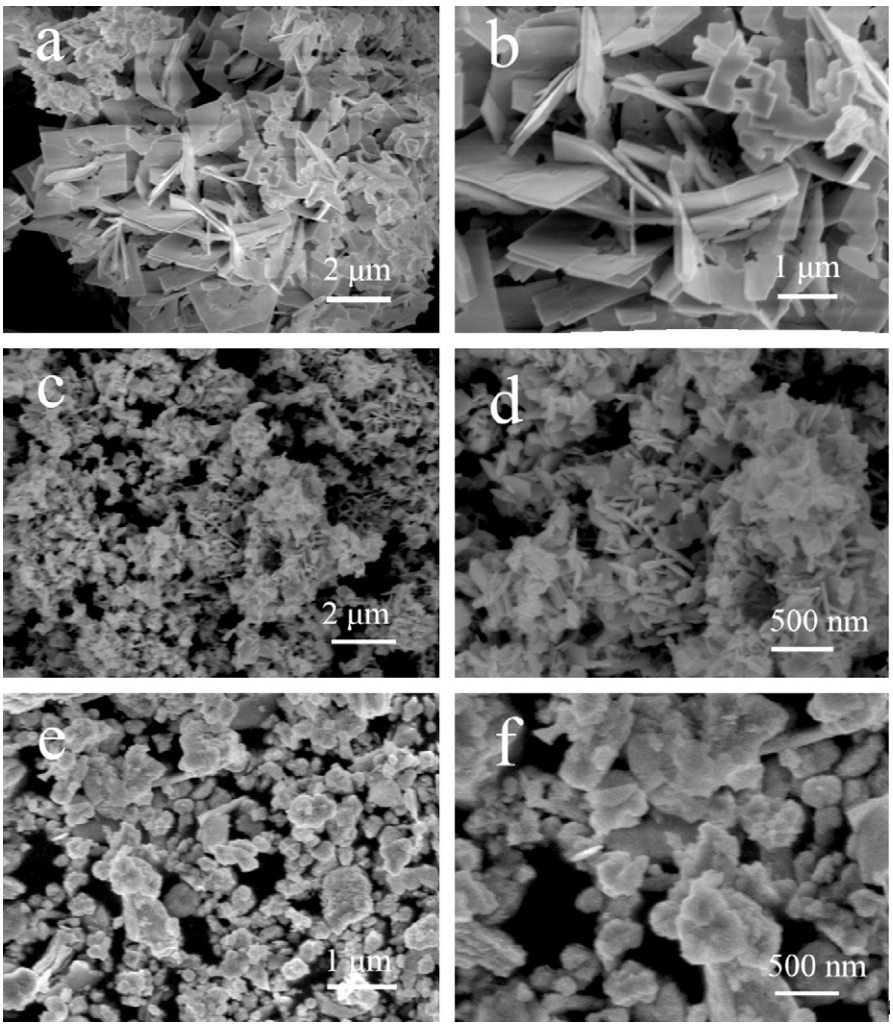

Fig. 5. FE-SEM images of bismuth tungstate products obtained at different pH values. (a) and (b) 7.0; (c) and (d) 9.0; (e) and (f) 11.0.

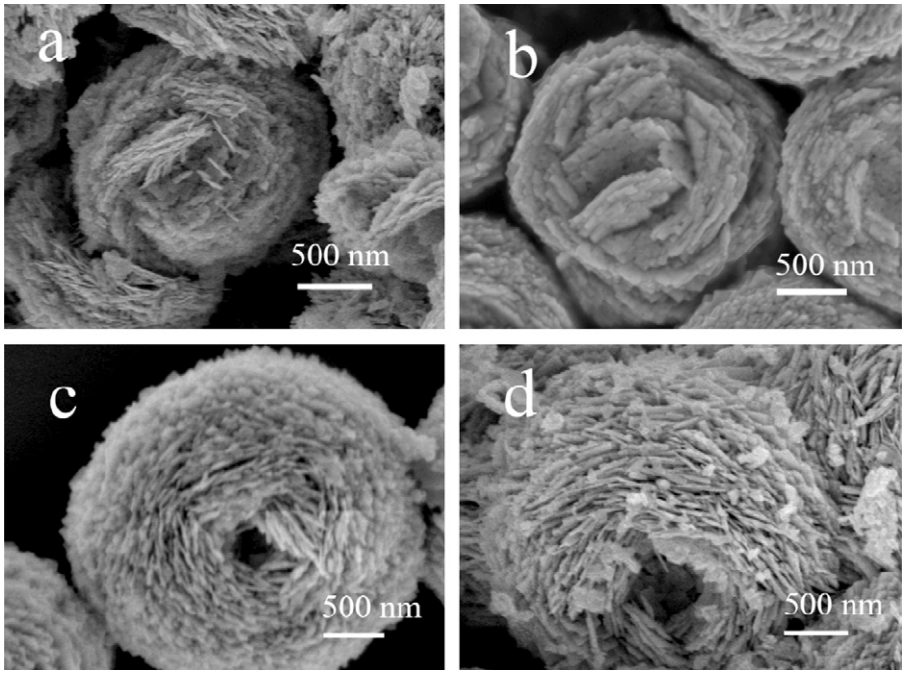

Fig. 6. FE-SEM images of the nest-like Bi_2WO_6 hierarchical nano/microstructures synthesized from different amount of CTAB. (a) 0.0 g, (b) 0.2 g, (c) 0.5 g and (d) 1.0 g.

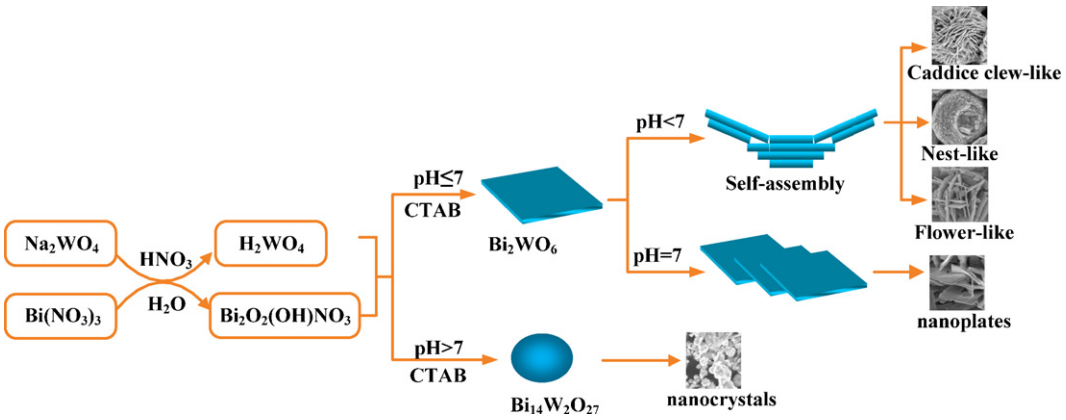

Fig. 7. Schematic illustration for the growth mechanism of as-synthesized products under different pH conditions.

ble H_2WO_4, which further determines the rates of nucleation and the assembly manners of Bi_2WO_6 nanoplates. In the strong acidic conditions (pH 0.5 and 2.0), the H_2WO_4 precipitate are formed richly in the precursor solution, causing the rapid hydrolysis of $Bi(NO_3)_3$ as shown in Eqs. (2) and (3). This promotes substantially the nucleation of Bi_2WO_6. The large numbers of nucleation centers of Bi_2WO_6 benefit the formation of the caddice clew-like and nest-like Bi_2WO_6 hierarchical nano/microstructures. It can be attributed to that the rich matter source and the low diffusion free path make the preferential growth of Bi_2WO_6 nanoplates be prevented. At weak acidic conditions (pH 4), the output of H_2WO_4 precipitate decreases, so that the nucleation centers reduces and the diffusion free path increases, which benefit the preferential growth of Bi_2WO_6 nanoplates. As a result, flower-like nano/microstructures were formed. When pH ≥ 7, the H_2WO_4 precipitate decreases substantially and the second phase $Bi_{14}W_2O_{27}$ appears due to the high solubility of WO_4^{2-} in alkaline solution. The corresponding reaction takes place as in Eq. (5). The long diffusion free path makes the reactants reach rapidly the high energy surfaces to present the preferential and directional growth of Bi_2WO_6 in the (0 2 0) direction. This leads to two-dimensional growth of Bi_2WO_6 to form plates of Bi_2WO_6. Obviously, with the increasing of the pH value, the assembly of Bi_2WO_6 behaves inactive and prefers to form two-dimensional structures. Therefore, the controlled growth of Bi_2WO_6 morphologies can be modulated by the pH value of the precursor solution.

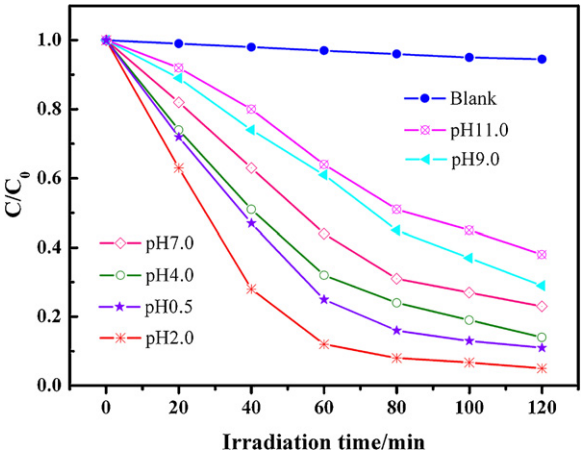

Fig. 8. Photodegradation efficiencies of RhB by as-synthesized products (blank: the blank test) under visible light irradiation.

3.4. Photocatalytic properties

Fig. 8 shows the photocatalytic efficiencies of RhB by the as-prepared Bi_2WO_6 nano/microstructures. The blank test demonstrates that the degradation of RhB is extremely slow without photocatalyst. The samples obtained in the solutions with pH values from 0.5 to 11.0 exhibit the photocatalytic efficiencies as 88.7%, 91.2%, 82.5%, 63.9%, 56.4% and 43.1%, respectively. The various photocatalytic activities should be due to the difference in band gap energy and the BET surface areas resulting from their distinct morphologies. In our case, the band gap energy is estimated to be about 2.68, 2.61, 2.70, 2.76, 2.79 and 2.83 eV for samples prepared at pH 0.5, 2.0, 4.0, 7.0, 9.0 and 11.0, respectively. Therefore, the enhanced photocatalytic activity of the nest-like Bi_2WO_6 nano/microstructure can be attributed not only to its strong absorption of visible light due to the band gap, but also to the BET surface area (35.2 $m^2\ g^{-1}$) which is much higher than that of other samples. In addition, the photocatalytic efficiencies decrease drastically associated with the phase transition from the Bi_2WO_6 to the $Bi_{14}W_2O_{27}$. It suggests that the crystal type may affect the photocatalytic activities predominantly in these samples. This is consistent with the previous report that $Bi_{14}W_2O_{27}$ possesses little photocatalytic activity under visible light irradiation [28].

4. Conclusions

In summary, bismuth tungstate nano/microstructures with different morphologies were successfully synthesized in a simple hydrothermal process by adjusting the pH value of precursor solutions. It was found that the pH value significantly influenced the structure and crystal phase of the obtained bismuth tungstate samples. The pH value of the solution was considered as the key factor to influence the assembling manner of Bi_2WO_6. The formation mechanism of different morphologies of Bi_2WO_6 was investigated, which would be helpful for providing a deeper understanding of crystal growth during the hydrothermal process. The photocatalytic activities of different products were closely related to their unique morphologies.

Acknowledgments

This work was financially supported by a grant from the Major State Basic Research Development Program of China (973 Program) (Grant No. 2007CB936601).

References

[1] Y.M. Sui, W.Y. Fu, H.B. Yang, Y. Zeng, Y.Y. Zhang, Q. Zhao, Y.G. Li, X.M. Zhou, Y. Leng, M.H. Li, G.T. Zou, Cryst. Growth Des. 10 (2010) 99.
[2] F. Li, J.F. Wu, Q.H. Qin, Z. Li, X.T. Huang, J. Alloys Compd. 492 (2010) L44.
[3] Z.G. Cheng, S.Z. Wang, D.J. Si, B.Y. Geng, J. Alloys Compd. 492 (2010) 339.
[4] L.D. Zhang, M. Fang, Nano Today 5 (2010) 128.
[5] X.X. Ji, X.T. Huang, J.P. Liu, J. Jiang, X. Li, R.M. Ding, Y.Y. Hu, F. Wu, Q. Li, J. Alloys Compd. 503 (2010) L21.
[6] A. Boukhachem, S. Fridjine, A. Amlouk, K. Boubaker, M. Bouhafs, M. Amlouk, J. Alloys Compd. 501 (2010) 339.
[7] J. Yan, X.S. Fang, L.D. Zhang, Y. Bando, U.K. Gautam, B. Dierre, T. Sekiguchi, D. Golberg, Nano Lett. 8 (2008) 2794.
[8] J.H. Ahn, G.X. Wang, Y.J. Kim, H.M. Lee, H.S. Shin, J. Alloys Compd. 504S (2010) S361.
[9] X.S. Fang, Y. Bando, U.K. Gautam, C.H. Ye, D. Golberg, J. Mater. Chem. 18 (2008) 509.
[10] J.M. Wang, P.S. Lee, J. Ma, Cryst. Growth Des. 9 (2009) 2293.
[11] Q.L. Li, Y.F. Wang, C.B. Chang, J. Alloys Compd. 505 (2010) 523.
[12] P.F. Hu, D.Z. Jia, Y.L. Cao, Y.D. Huang, L. Liu, J.M. Luo, Nanoscale Res. Lett. 4 (2009) 437.
[13] S. Asokan, K.M. Krueger, V.L. Colvin, M.S. Wong, Small 3 (2007) 1164.
[14] X.S. Fang, Y. Bando, G.Z. Shen, C.H. Ye, U.K. Gautam, P.M. Costa, C.Y. Zhi, C.C. Tang, D. Golberg, Adv. Mater. 19 (2007) 2593.
[15] J. Li, X.S. Tang, Z.Y. Lu, Y.T. Qian, J. Alloys Compd. 497 (2010) 390.
[16] G.M. Hua, Y. Tian, L.L. Yin, L.D. Zhang, Cryst. Growth Des. 9 (2009) 4653.
[17] J.Y. Xiang, J.P. Tu, L. Zhang, Y. Zhou, X.L. Wang, S.J. Shi, J. Power Sources 195 (2010) 313.
[18] G.L. Tan, J.H. Du, Q.J. Zhang, J. Alloys Compd. 468 (2009) 421.
[19] D.N. Ke, T.Y. Peng, L. Ma, P. Cai, K. Dai, Inorg. Chem. 48 (2009) 4685.
[20] J. Wu, F. Duan, Y. Zheng, Y.J. Xie, Phys. Chem. C 111 (2007) 12866.
[21] L.S. Zhang, W.Z. Wang, Z.G. Chen, H.L. Xu, Small 3 (2007) 1618.
[22] C. Zhang, Y.F. Zhu, Chem. Mater. 17 (2005) 3537.
[23] L.S. Zhang, W.Z. Wang, Z.G. Chen, L. Zhou, H.L. Xu, W. Zhu, J. Mater. Chem. 17 (2007) 2526.
[24] D.K. Ma, S.M. Huang, W.X. Chen, S.W. Hu, F.F. Shi, K.L. Fan, J. Phys. Chem. C 113 (2009) 4369.
[25] C.X. Xu, X. Wei, Z.H. Ren, Y. Wang, G. Xu, G. Shen, G.R. Han, Mater. Lett. 63 (2009) 2194.
[26] L. Zhou, W.Z. Wang, L.S. Zhang, J. Mol. Catal. A: Chem. 268 (2007) 195.
[27] X.J. Dai, Y.S. Luo, W.D. Zhang, S.Y. Fu, Dalton Trans. 39 (2010) 3426.
[28] H.D. Xie, D.Z. Shen, X.Q. Wang, G.Q. Shen, Mater. Chem. Phys. 103 (2007) 334.